ORIGINAL PAPER

Active nonlinear energy sink using force feedback under transient regime

G. Zhao [ORCID] · **G. Raze** · **A. Paknejad** · **A. Deraemaeker** · **G. Kerschen** ·
C. Collette

Abstract In this paper, an active nonlinear energy
sink (ANES) based on force feedback is investigated.
The proposed device is composed of a pair of
collocated actuator and force sensor. The control law
is implemented by feeding back the output of the force
sensor, through one single integrator and one double
integrator of its cube. Its working principle can be
understood by an equivalent mechanical network
which consists of a linear dashpot, linear spring and
a cube root inerter. Although the nonlinear assignment
between the spring and mass or inerter quantities is
different from that of traditional nonlinear energy
sinks (NESs), it is found that ANES and NES behave
similarly in terms of their slow-scale dynamics and the
vibration mitigation effectiveness. Closed-form
expressions for properly tuning the feedback gains
are derived. Numerical simulations are performed to
validate the analytical analysis. The damping
mechanism of ANES through targeted energy transfer
and resonance capture cascade is demonstrated.

Keywords Inerter · Force feedback · Nonlinear
energy sink · Targeted energy transfer · Resonance
capture cascade

G. Zhao (✉) · A. Paknejad · C. Collette
Precision Mechatronics Laboratory, Beams Department,
Université Libre de Bruxelles, F.D. Roosevelt Av 50,
1050 Brussels, Belgium
e-mail: guoying.zhao@ulb.ac.be

G. Raze · G. Kerschen · C. Collette
Department of Aerospace and Mechanical Engineering,
University of Liège, Allée de la Découverte 9,
4000 Liège, Belgium

A. Deraemaeker
BATir Department, Université Libre de Bruxelles, F.D.
Roosevelt Av 50, 1050 Brussels, Belgium

1 Introduction

Lightweight materials have been more and more used
for system constructions in many engineering appli-
cations for the sake of fuel efficiency and reduction of
environmental pollution [1, 2]. However, this will
often make these structures lightly damped and
responses could be unacceptably amplified around
the resonance, causing many problems such as reduc-
tion in structural integrity, compromise of instrument
functionality and even threat to human lives. In this
sense, proper damping techniques need to be consid-
ered in parallel with the future design of lightweight
structures. A tuned mass damper (TMD) [3] which
typically consists of a proof mass and a spring-dashpot
pair is often employed for such purpose. It acts as an
auxiliary system to the host structures where addi-
tional damping is needed. The natural frequency of the
added TMD is often suggested to be roughly equal to
one of the resonance frequencies of the host structure
[4]. In this way, the vibration energy associated with
the considered mode can be quickly transferred and

localised in the TMD where it is eventually dissipated. Due to this nature, TMDs are only effective around one particular vibration mode. Deviation from the desired settings can also degrade their performance [5]. In addition, one single TMD is only capable of dealing with one specified vibration mode to which it is tuned.

An interesting nonlinear damping alternative, i.e., a nonlinear energy sink (NES) was proposed aiming to overcome these limitations [6, 7]. A NES is often realised by a proof mass, a dashpot and a cubic nonlinear spring. The working principle of NESs is a bit different from that of TMDs, the host structure energy is in fact irreversibly transferred to NESs and dissipated therein. As there are only nonlinear resilient elements within NESs, the natural frequency is not essentially fixed but is rather dependent on the vibration amplitude. This allows NESs to interact basically with every mode of the host structure and also makes them insensitive to parameter variations of the host structure. Substantial work has been done to better understand the underlying dynamics of NESs, see for example [8–13]. In the transient regime, it has been illustrated that there exists a threshold in terms of the vibration energy level of the host structure above which NESs start to work efficiently, i.e. where targeted energy transfer (TET) occurs. TET is defined as a one-way irreversible transfer of energy from the host structure to the NES. Some design guidelines for properly choosing the parameters, namely the nonlinear stiffness and the damping coefficient to initiate TET, have been established [12, 14]. Other possibilities for implementing NESs than using a cubic nonlinear spring have been also explored [15, 16]. As for the last parameter of NESs, a heavier proof mass is preferable, similarly to that for TMDs. However, the added mass may be penalising in light weight applications, e.g. automotive and aerospace structures. Zhang et al. [17] and Javidialesaadi and Wierschem [18] proposed to integrate inerters into NESs aiming to boost the performance as the inertance of inerters can be significantly greater than their actual mass [19, 20]. Although the potential of NESs is promising, it is quite challenging to realise them in practice because attaching them to the host structure with a pure cubic spring without any linear resilient parts remains a challenge.

In order to bypass the aforementioned practical issues, an active nonlinear sink using a novel force feedback controller is proposed in this work. A force sensor is chosen since the control plant for the corresponding underlying linear active system always possesses alternating poles and zeros, which would ease the design concern on the stability of the closed loop [21]. The control law is formed by feeding back the output of the force sensor through one single integrator and one double integrator of its cube. The control concept is actually built upon the previous developments [22] where the linear double integrator is removed from the chain. In this way, the proposed ANES can be understood to play the same role as a pure mechanical system which consists of a cube root inerter, a linear dashpot and a linear spring according to previous derivations in [22–24]. Although the nonlinear assignment of the proposed ANES is different from that of traditional NESs, it is found that ANES and NES behave similarly in terms of vibration mitigation effectiveness. Some other interesting work dealing with control of nonlinear systems can be found in [25–27]. The principal contributions of the work presented are: (a) the development of the equivalent mechanical model which enables a straightforward interpretation of the physics behind the active control law, (b) the derivation of the ANES tuning law in closed-form, and (c) the equivalence examination between an ANES and a mechanical NES which opens the door for the real-time tuning of control parameters of an active nonlinear energy sink.

The rest of paper is organised as follows. In the next section, the mathematical model of the system under consideration is developed. In Sect. 3, the tuning law of ANES for a single-degree-of-freedom (SDOF) system is derived and numerically verified. This tuning law is extended to a multi-degree-of-freedom system (MDOF) in Sect. 4. Conclusions are drawn in Sect. 5.

2 Mechanical representation of an ANES

The system under investigation is shown in Fig. 1a. It represents a linear MDOF system which is equipped with a massless actuator whose stiffness is denoted by k_a. A collocated force sensor which measures the transmission force denoted by F_s is installed between the actuator and the primary structure. The control loop is implemented by feeding the output of the force sensor F_s through a nonlinear controller $u(F_s)$ to drive
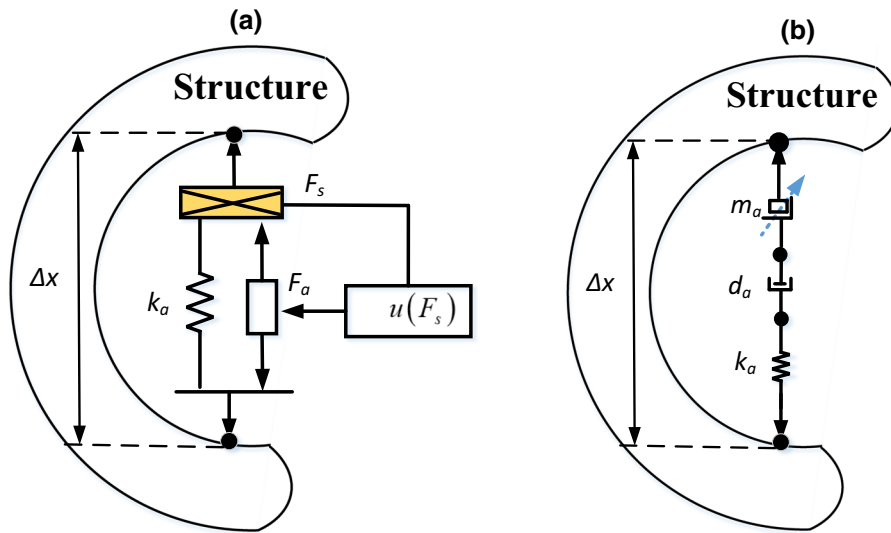
Fig. 1 **a** The sketch of the coupled system and **b** its equivalent mechanical representation

the actuator. In this work, the transient behaviour of the system is of interest and no external disturbance force is applied.

The governing equations of the coupled system can be written as:

$$\mathbf{M}\ddot{\mathbf{X}}(t) + \mathbf{C}\dot{\mathbf{X}}(t) + \mathbf{K}\mathbf{X}(t) = \mathbf{b}F_s(t) \tag{1}$$

$$F_s(t) = u(F_s(t)) - k_a\mathbf{b}^{\mathbf{T}}\mathbf{X}(t) \tag{2}$$

where $\mathbf{M} \in \Re^{n \times n}$, $\mathbf{C} \in \Re^{n \times n}$ and $\mathbf{K} \in \Re^{n \times n}$ represent the mass, damping and stiffness matrix, respectively, $\mathbf{X} \in \Re^{n \times 1}$ the displacement vector, $\mathbf{b} = [0 \quad \cdots \quad -1_l \quad 0 \quad \cdots \quad 1_k \quad \cdots \quad 0] \in \Re^{n \times 1}$ the actuator connection vector and F_s a scalar representing the force that acts on the structure (measured by the force sensor). Note that in the considered sketch the actuator is mounted to the primary structure through two attachment points where a pair of control forces are injected into the primary structure. Alternatively, the actuator can be also placed between the ground and the primary structure such that there is only one attachment point. In this case, a point control force is applied by the actuator. The two configurations make no difference in terms of the working principle of the ANES, but the connection vector $\mathbf{b}$ has to be adapted accordingly such that the ANES parameters can be correctly configured.

Note that the mass of the transducer is tacitly neglected in the paper. As a result, the validity of Eq. (1) should be restricted to frequencies well below

the resonance frequencies of the transducer. In addition, lumped masses of the transducer can be included at the associated DOFs to compensate statically the shift of the resonance frequencies when the mass of the transducer is relatively large.

The nonlinear controller $u(F_s)$ is built upon the controllers proposed in [22, 23], but modified to have a dynamic behaviour similar to that of NESs. The controller $u(F_s)$ reads:

$$u(F_s) = -g_s \int_0^t F_s \mathrm{d}t - g_{d3} \int_0^t \int_0^t F_s^3 \mathrm{d}t\mathrm{d}t \tag{3}$$

The working principle of the proposed controller can be better understood from a pure mechanical point of view. As illustrated in Appendix A, the function of the component with the single integrator in Eq. (3) behaves as a mechanical dashpot, and that with the double integrator resembles a cube root inerter. Together with the inherent spring of the actuator, the active system can be represented by a pure mechanical network composed by a linear spring, a linear dashpot and a cube root inerter connected in series. As such, the equivalent mechanical representation of the considered system is shown in Fig. 1b. The equivalent damping coefficient and the inertance are linked with the feedback gains according to:

$$d_a = k_a/g_s; \quad m_{a3} = \sqrt[3]{k_a/g_{d3}} \tag{4}$$

Because of the full analogy with a mechanical network, the stability of the active system is guaranteed given idealised force sensors and actuators are employed. According to the Lyapunov's linearisation theory [28], the actual nonlinear system is asymptotically stable at the equilibrium point if the corresponding linearised system is strictly stable. For the proposed ANES, the linearised system around the trivial state corresponds to the primary structure coupled with a classical integral force feedback controller. As demonstrated in [24, 29], the theoretical gain margin is infinity and the phase margin is $\pi/2$ for the linearised system. However, the Lyapunov's linearisation theory is only valid for small range of motions around the equilibrium points (a local stability theorem) and it is not yet clear what are the boundary conditions for the linearisation approximations to hold (global stability theorem is needed). It is left for the subject of future work.

Although it is referred to as 'active nonlinear energy sink', it is actually implemented in a way different than that for NES. Within ANES, the mass-like quantity, i.e. the cube root inerter, is nonlinear and coupled with a linear spring and a dashpot in series, while a classical NES features a linear mass supported by a nonlinear spring and a linear dashpot. Despite this difference, it is found later in the paper that the working principle and the corresponding control effectiveness of the two devices are similar.

Substituting Eq. (3) into Eq. (2), and transforming the resulting governing equations into modal coordinates according to $\mathbf{X}(t) = \mathbf{EQ}(t)$ where $\mathbf{E} = \begin{bmatrix} \mathbf{e}_1 & \mathbf{e}_2 & \cdots & \mathbf{e}_n \end{bmatrix} \in \Re^{n \times n}$ is the matrix of mode shapes and $\mathbf{Q} \in \Re^{n \times 1}$ the associated modal coordinates yields:

$$\mathbf{M}_q\ddot{\mathbf{Q}}(t) + \mathbf{C}_q\dot{\mathbf{Q}}(t) + \mathbf{K}_q\mathbf{Q}(t) = \mathbf{E}^T\mathbf{b}F_s(t) \qquad (5)$$

$$F_s(t) = -g_s\int_0^t F_s\mathrm{d}t - g_{d3}\int_0^t\int_0^t F_s^3\mathrm{d}t\mathrm{d}t - k_a\mathbf{b}^T\mathbf{EQ}(t) \qquad (6)$$

where $\mathbf{M}_q = \mathbf{E}^T\mathbf{ME}$ is the diagonal modal mass matrix, $\mathbf{K}_q = \mathbf{E}^T\mathbf{KE}$ the diagonal modal stiffness matrix and $\mathbf{C}_q = \mathbf{E}^T\mathbf{CE}$ the diagonal modal damping matrix assuming that the primary structure is lightly damped and $\mathbf{C}$ is considered to be proportional to $\mathbf{M}$ and $\mathbf{K}$ ($\mathbf{C} = \alpha\mathbf{M} + \beta\mathbf{K}, \quad \alpha, \beta \in \Re_+$).

Consider now that the system only vibrates at the resonance frequency associated with mode i such that $\mathbf{X}(t) = \mathbf{EQ}(t) = \sum_{m=1}^n \mathbf{e}_m q_m(t) \approx \mathbf{e}_i q_i(t)$ is valid. Equations (5) and (6) can be thus rewritten as:

$$m_{q,i}\ddot{q}_i(t) + c_{q,i}\dot{q}_i(t) + k_{q,i}q_i(t) = f_{s,i}(t) \qquad (7)$$

$$f_{s,i}(t) = -g_s\int_0^t f_{s,i}\mathrm{d}t - g_{d3,i}\int_0^t\int_0^t (f_{s,i})^3\mathrm{d}t\mathrm{d}t \\ - k_{a,i}q_i(t) \qquad (8)$$

where $\Delta e_i = \mathbf{e}_i(l) - \mathbf{e}_i(k)$, $f_{s,i} = \Delta e_i F_s(t)$, $g_{d3,i} = g_{d3}/\Delta e_i^2$ and $k_{a,i} = k_a\Delta e_i^2$.

The characteristic equations defined by Eqs. (7) and (8) actually correspond to a system as depicted in Fig. 2a. This system is defined through a lumped mass $m_{q,i}$ suspended from the ground by a linear spring $k_{q,i}$, a dashpot $c_{q,i}$ and the actuator whose stiffness is denoted by $k_{a,i}$. The variables $m_{q,i}$, $k_{q,i}$ and $c_{q,i}$ represent the modal mass, stiffness and damping coefficient of the primary structure for mode i, while $f_{s,i}$, $g_{d3,i}$, $g_{d3,i}$ and $k_{a,i}$ are the corresponding equivalent transmission force, the nonlinear feedback gain, the linear feedback gain and the actuator stiffness of the ANES for mode i. The corresponding equivalent mechanical model is given in Fig. 2b. In the forthcoming section, the simplified system in Fig. 2a will be used to study the ANES characteristics with the aim to derive practical guidelines for the design of an effective ANES.

3 ANES tuning for SDOF systems

3.1 Semi-analytic reduction

The parameters:

$$\begin{aligned} & x_1 = q_i, & x_2 = f_{s,i}/k_{a,i}, & \omega_i = \sqrt{k_{q,i}/m_{q,i}}, & \tau = \omega_i t, \\ & \varepsilon = k_{a,i}/k_{q,i}, & \xi_1 = c_{q,i}\omega_1/k_{a,i}, & g^{sn} = g_s/\omega_i, & g^{3n} = g_{d3,i}(k_{a,i})^2 / \omega_i^2 \end{aligned} \qquad (9)$$

are introduced to normalise the governing equations Eqs. (7) and (8):

$$x_1'' + \varepsilon\xi_1 x_1' + x_1 - \varepsilon x_2 = 0 \qquad (10)$$

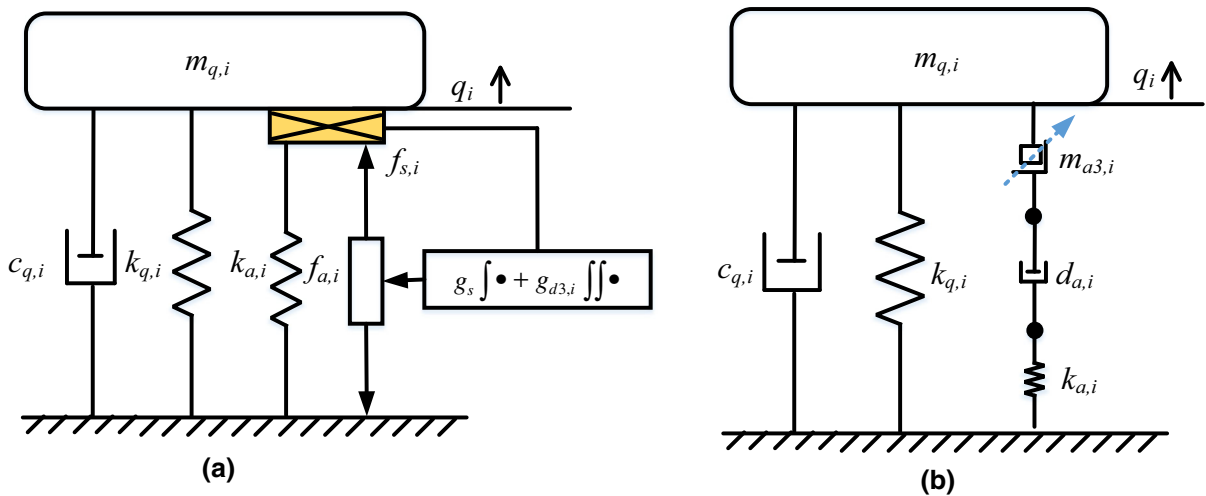$$x_2'' + g^{sn}x_2' + g^{3n}x_2^3 + x_1'' = 0 \qquad (11)$$

Fig. 2 **a** The representative model of the whole system for one vibration mode and **b** its equivalent mechanical model

where $'$ denotes derivation with respect to (w.r.t.) the time scale τ.

Under the assumption of 1:1 resonance and the system vibrates along mode i, complex variables are introduced to reduce the order of the differential equations [30]:

$$\phi_1(\tau)e^{j\tau} = x_1' + jx_1; \quad \phi_2(\tau)e^{j\tau} = x_2' + jx_2 \tag{12}$$

where $j = \sqrt{-1}$.

Substituting Eq. (12) into Eqs. (10) and (11) yields:

$$\phi_1'e^{j\tau} - \varepsilon\frac{\phi_2 e^{j\tau} - \phi_2^* e^{-j\tau}}{2j} + \varepsilon\xi_1\frac{\phi_1 e^{j\tau} + \phi_1^* e^{-j\tau}}{2} = 0 \tag{13}$$

$$\phi_1'e^{j\tau} + \phi_2'e^{j\tau} - \frac{\phi_1 e^{j\tau} - \phi_1^* e^{-j\tau} + \phi_2 e^{j\tau} - \phi_2^* e^{-j\tau}}{2j}$$
$$+ g^{sn}\frac{\phi_2 e^{j\tau} + \phi_2^* e^{-j\tau}}{2} + g^{3n}j\frac{\left(\phi_2 e^{j\tau} - \phi_2^* e^{-j\tau}\right)^3}{8}$$
$$= 0 \tag{14}$$

where $*$ denotes complex conjugate.

Each complex variable is decomposed into power series of the stiffness ratio ε ($\varepsilon \ll 1$) as follows:

$$\phi_i = \phi_{i0} + \varepsilon\phi_{i1} + O(\varepsilon^2), \forall i = 1, 2 \tag{15}$$

where ϕ_{i0} is the dominant term and ϕ_{i1} the small perturbation term. Here, the expansions are truncated for $O(\varepsilon^2)$.

The multiple scales method [31] is applied to Eq. (15) to better approximate the system dynamics. This method assumes that the dynamics behave according to several discrete time scales. In this paper, $\tau_0 = \tau$ and $\tau_1 = \varepsilon\tau$ representing the fast and the slow time scales are considered; they are related to the original time scale as:

$$\frac{d}{d\tau} = \frac{\partial}{\partial\tau_0} + \varepsilon\frac{\partial}{\partial\tau_1} \tag{16}$$

Substituting Eqs. (15) and (16) into Eqs. (13) and (14), one obtains:

$$\frac{\partial\phi_{10}}{\partial\tau_0} + \varepsilon\frac{\partial\phi_{10}}{\partial\tau_1} + \varepsilon\frac{\partial\phi_{11}}{\partial\tau_0} + \varepsilon^2\frac{\partial\phi_{11}}{\partial\tau_1} + \frac{j\varepsilon(\phi_{20} + \varepsilon\phi_{21})}{2}$$
$$+ \frac{\varepsilon\xi_1(\phi_{10} + \varepsilon\phi_{11})}{2}$$
$$= 0 \tag{17}$$

where the secular terms w.r.t. the time scale τ_0 are eliminated.

Collecting the terms according to the different orders of the stiffness ratio ε in Eqs. (17) and (18), one obtains:

$$\frac{\partial \phi_{10}}{\partial \tau_0} + \varepsilon \frac{\partial \phi_{10}}{\partial \tau_1} + \varepsilon \frac{\partial \phi_{11}}{\partial \tau_0} + \varepsilon^2 \frac{\partial \phi_{11}}{\partial \tau_1} + \frac{\partial \phi_{20}}{\partial \tau_0} + \varepsilon \frac{\partial \phi_{20}}{\partial \tau_1} + \varepsilon \frac{\partial \phi_{21}}{\partial \tau_0} + \varepsilon^2 \frac{\partial \phi_{21}}{\partial \tau_1}$$

$$+ \frac{j(\phi_{10} + \varepsilon \phi_{11} + \phi_{20} + \varepsilon \phi_{21})}{2} + \frac{g^{sn}(\phi_{20} + \varepsilon \phi_{21})}{2}$$

$$- \frac{3 g^{3n} j \left(|\phi_{20}|^2 \phi_{20} + \varepsilon \left(2\phi_{21}|\phi_{20}|^2 + \phi_{20}^2 \phi_{21}^* \right) + \varepsilon^2 \left(2\phi_{20}|\phi_{21}|^2 + \phi_{20}^* \phi_{21}^2 \right) + \varepsilon^3 |\phi_{21}|^2 \phi_{21} \right)}{8} = 0 \tag{18}$$

$$\frac{\partial \phi_{10}}{\partial \tau_0} = 0 \Rightarrow \mathrm{O}(\varepsilon^0) \tag{19}$$

$$\frac{\partial \phi_{10}}{\partial \tau_0} + \frac{\partial \phi_{20}}{\partial \tau_0} + \frac{j(\phi_{10} + \phi_{20})}{2} + \frac{g^{sn}\phi_{20}}{2} - \frac{3g^{3n}\phi_{20}|\phi_{20}|^2 j}{8} = 0 \Rightarrow \mathrm{O}(\varepsilon^0) \tag{20}$$

$$\frac{\partial \phi_{10}}{\partial \tau_1} + \frac{\partial \phi_{11}}{\partial \tau_0} + \frac{j\phi_{20}}{2} + \frac{\xi_1 \phi_{10}}{2} = 0 \Rightarrow \mathrm{O}(\varepsilon^1) \tag{21}$$

Equation (19) means that the leading variable ϕ_{10} does not depend on τ_0. This indicates that $\phi_{10}(\tau_0, \tau_1)$ can be approximated using only its slowly-varying component $\phi_{10}(\tau_1)$. Substituting Eq. (19) into Eq. (20), the resulting expression describes how ϕ_{20} evolves w.r.t. the time scale τ_0. For this one-dimensional system, it was shown in [32] that ϕ_{20} ultimately converge to the steady-state solutions of Eq. (20) as:

$$\frac{j(\phi_{10} + \phi_{20})}{2} + \frac{g^{sn}\phi_{20}}{2} - \frac{3g^{3n}\phi_{20}|\phi_{20}|^2 j}{8} = 0 \tag{22}$$

Note that the solutions of Eq. (22) neglect the transient dynamics of $\phi_{20}(\tau_0, \tau_1)$ at the fast time scale, which also means that they are sought by taking the limit $\tau_0 \to \infty$.

Proceeding now to Eq. (21) and taking the above ansatz $\tau_0 \to \infty$, the secular term w.r.t. the time scale τ_0, i.e. $\frac{\partial \phi_{11}}{\partial \tau_0}$, is omitted and one obtains:

$$\frac{\partial \phi_{10}}{\partial \tau_1} + \frac{j\phi_{20}}{2} + \frac{\xi_1 \phi_{10}}{2} = 0 \tag{23}$$

Up to now, it is possible to solve the slowly-varying components $\phi_{10}(\tau_1)$ and $\phi_{20}(\tau_1) = \lim_{\tau_0 \to \infty} \phi_{20}(\tau_0, \tau_1)$ from Eqs. (22) and (23). Specifically, $\phi_{20}(\tau_1)$ represents the trend of ϕ_{20} after eliminating the fast oscillations.

In order to further simplify the analysis, a polar decomposition of the complex variables is introduced:

$$\phi_{10} = R_1(\tau_1) e^{j\delta_1(\tau_1)}, \quad \phi_{20} = R_2(\tau_1) e^{j\delta_2(\tau_1)} \tag{24}$$

where $R_i \in \Re_+$ is the amplitude of ϕ_i, and δ_i the corresponding phase.

Substituting Eq. (24) into Eqs. (22) and (23) yields:

$$\frac{\partial R_1}{\partial \tau_1} - \frac{R_2 \sin(\delta_2 - \delta_1)}{2} + \frac{\xi_1 R_1}{2} = 0 \tag{25}$$

$$\frac{\partial \delta_1}{\partial \tau_1} R_1 + \frac{R_2 \cos(\delta_2 - \delta_1)}{2} = 0 \tag{26}$$

$$\frac{R_1 \cos(\delta_1 - \delta_2) + R_2}{2} + \frac{3R_2^3 g^{3n}}{8} = 0 \tag{27}$$

$$\frac{-R_1 \sin(\delta_1 - \delta_2)}{2} + \frac{R_2 g^{sn}}{2} = 0 \tag{28}$$

Eliminating the phase difference $\delta_1 - \delta_2$ from Eqs. (27) and (28) gives:

$$R_1^2 = R_2^2 \left((g^{sn})^2 + \left(1 - \frac{3}{4} g^{3n} R_2^2 \right)^2 \right) \tag{29}$$

Taking the expression for $\sin(\delta_1 - \delta_2)$ in Eq. (28) and substituting it into Eq. (25), one obtains:

$$\frac{\partial R_1}{\partial \tau_1} R_1 = -\frac{g^{sn} R_2^2}{2} - \frac{\xi_1 R_1^2}{2} \tag{30}$$

Further simplifications can be made by taking $E_k = R_k^2, \forall k = 1, 2$ which gives:

$$E_1 = |\phi_{10}|^2 = (x_1')^2 + x_1^2 + \mathrm{O}(\varepsilon^1) \tag{31}$$

$$E_2 = |\phi_{20}|^2 = \lim_{\tau_0 \to \infty} \left((x_2')^2 + x_2^2 + \mathrm{O}(\varepsilon^1) \right) \tag{32}$$

Variables E_1 and E_2 play a similar role similar to the normalised energy of the primary structure and the attached active system, respectively.

Substituting Eqs. (31) and (32) into Eqs. (30) and (29), the system dynamics are governed by:

$$\frac{\partial E_1}{\partial \tau_1} = -\xi_1 E_1 - g^{sn} E_2 \qquad (33)$$

$$E_1 = E_2 \left((g^{sn})^2 + \left(1 - \frac{3}{4} g^{3n} E_2 \right)^2 \right) \qquad (34)$$

Equation (33) describes how the energy-like quantities E_1 and E_2 dynamically evolve w.r.t. the slow time scale τ_1, while Eq. (34) regulates them statically. Because the normalised damping factors ξ_1 and g^{sn} as well as E_1 and E_2 are positive variables, the gradient of the primary structure energy E_1 w.r.t. the slow time scale is always negative, as seen from Eq. (33). This means that the primary structure's energy will always be dissipated over the slow flow time. On the other hand, the evolution of E_2 is governed by E_1 following a nonlinear algebraic expression Eq. (34) where only the control parameters g^{sn} and g^{3n} are present. Thanks to this nonlinear relation, TET from the primary structure to the ANES can occur. The semi-analytic governing Eqs. (33) and (34) are identical to those obtained in [14] for a mechanical NES provided the time scale in [14] is changed to a dimensionless quantity w.r.t. the resonance frequency of the primary structure. From this perspective, the normalised feedback gains g^{sn} and g^{3n} play the same role as the damping ratio and the nonlinear frequency ratio associated with a mechanical NES. This is logical as they correspond to a normalised dashpot and cube root inerter, respectively. We also note that switching nonlinear assignments between the spring and mass or inerter quantities does not significantly change the control effectiveness of the resulting device if one compares the active nonlinear inerter damper in [22] with the nonlinear tuned mass damper in [33]. However, it should be noticed that E_1 and E_2 in this paper correspond to the absolute motion of the primary mass and the transmission force induced by an ANES, while for the mechanical NES they are related to the motion of the centre of mass and the relative motion between the primary and NES masses. Despite this difference, the tuning law of an ANES that triggers

TET based on Eqs. (33) and (34) is foreseen to be the similar to that obtained as in [14].

Two new variables $Z_1 = g^{3n} E_1$ and $Z_2 = g^{3n} E_2$ are now introduced. In addition, the damping factor of the primary structure is omitted. Equations (33) and (34) are thus rewritten as:

$$\frac{\partial Z_1}{\partial \tau_1} = -g^{sn} Z_2 \qquad (35)$$

$$Z_1 = Z_2 \left((g^{sn})^2 + \left(1 - \frac{3}{4} Z_2 \right)^2 \right) \qquad (36)$$

In order to better study the underlying dynamics, Eq. (36) is differentiated w.r.t. Z_2, which gives:

$$\begin{aligned} \frac{\partial Z_1}{\partial Z_2} &= \frac{27}{16} Z_2^2 - 3Z_2 + 1 + (g^{sn})^2 \\ &= 3 \left(\frac{3}{4} Z_2 - \frac{2}{3} \right)^2 - \frac{1}{3} + (g^{sn})^2 \end{aligned} \qquad (37)$$

Equation (37) is a quadratic equation which is always positive if $g^{sn} > \sqrt{1/3}$. If this is the case, Z_1 will monotonically increase/decrease with an increase/decrease of Z_2. Because Eq. (35) indicates that Z_1 is always reduced w.r.t. the slow time scale, Z_2 will follow the same trend whereby no energy is fed into the ANES and thus no TET occurs. If $g^{sn} < \sqrt{1/3}$, Eq. (37) has two roots Z_2^{1*} and Z_2^{2*} ($Z_2^{1*} < Z_2^{2*}, \forall Z_2^{i*} \in \Re_+, i = 1, 2$). It remains positive when Z_2 is either smaller than Z_2^{1*} or greater than Z_2^{2*}. Otherwise, Eq. (37) becomes negative meaning that the energy in the primary structure and in the ANES can flow in opposite ways. In this case, when plotted against $Z_2 : 0 \to \infty$, Z_1 exhibits a maximum followed by a minimum due to the changing sign of its derivative w.r.t. Z_2; it is initially positive, then negative and finally positive again. In addition, three solutions of Z_2 can be found for Z_1 bounded between the two extrema. In summary, TET can occur as discussed in [14, 15] provided that:

$$g^{sn} < \sqrt{\frac{1}{3}} \qquad (38)$$

The solutions to Eq. (37), i.e. Z_2^{1*} and Z_2^{2*}, and the corresponding extreme values can be derived:
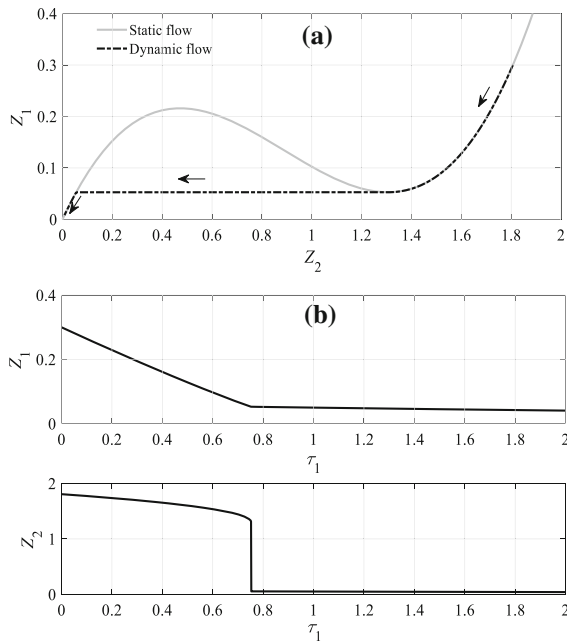
Fig. 3 **a** Slow invariant manifold of Z_1 and Z_2 when g^{sn} is set to 0.2 and Z_1^{init} is set to 0.3, **b** the corresponding time history of Z_1 and Z_2 at slow time scale

$$Z_1^{\max} = \frac{8}{81}\left[4 - \left(1 - 3(g^{sn})^2\right)\left(3 - \sqrt{1 - 3(g^{sn})^2}\right)\right],$$
$$Z_2^{1*} = \frac{8}{9} - \frac{4\sqrt{1 - 3(g^{sn})^2}}{9}$$
(39)

$$Z_1^{\min} = \frac{8}{81}\left[4 - \left(1 - 3(g^{sn})^2\right)\left(3 + \sqrt{1 - 3(g^{sn})^2}\right)\right],$$
$$Z_2^{2*} = \frac{8}{9} + \frac{4\sqrt{1 - 3(g^{sn})^2}}{9}$$
(40)

Besides the condition imposed on g^{sn}, it was shown that the initial conditions of the system also play an important role in the TET mechanism [10, 14, 15]. Specifically, the initial energy of the primary structure Z_1^{init} has to be greater than $Z_1^{\max}$ given in Eq. (39). Figure 3a depicts the slow invariant manifold between Z_1 and Z_2 when the condition $Z_1^{\text{init}} > Z_1^{\max}$ is satisfied. As can be seen, Z_1 and Z_2 smoothly decrease from their initial conditions until Z_1 reaches its local minimum $Z_1^{\min}$. At that moment, Z_2 undergoes a jump, and is suddenly reduced from Z_2^{2*} to the smallest

solution of Z_2 corresponding to $Z_1^{\min}$. This jump phenomenon, however, is not observed for Z_1 which continues to decrease after $Z_1^{\min}$ but following a different branch, i.e. the leftmost branch of the invariant manifold. The evolution of Z_1 and Z_2 against the slow time scale τ_1 is shown in Fig. 3b. It is noted that Z_1 decays with a quasi-linear slope before the critical point $Z_1^{\min}$ instead of an exponential rate typically associated with linear systems. This clearly indicates the occurrence of TET. After the critical point $\left(Z_1^{\min}, Z_2^{2*}\right)$, TET vanishes and Z_1 decreases much slower compared to the case when TET is active. This drastically decreased rate is understood to be due to the low post-jump value of Z_2, which by virtue of Eq. (35) entails a low dissipation rate for Z_1. When the condition $Z_1^{\text{init}} > Z_1^{\max}$ is not valid, TET is not be robustly triggered or not triggered at all, as demonstrated in [14, 15].

In order to meet this condition, the minimal normalised control gain g^{3n}, i.e. the normalised cube root inertance can be derived as:

$$g^{3n}E_1^{\text{init}} = Z_1^{\text{init}} \geq Z_1^{\max}$$
$$\downarrow$$
$$g^{3n} \geq \frac{8}{81E_1^{\text{init}}}\left[4 - \left(1 - 3(g^{sn})^2\right)\left(3 - \sqrt{1 - 3(g^{sn})^2}\right)\right]$$
(41)

3.2 Influence of control parameters

Up to now, the tuning laws (38) and (41) for the two control parameters g^{sn} and g^{3n} that initiate TET have been derived. However, it is not yet clear what is their impact on the vibration mitigation performance. In this section, two metrics introduced in [14], namely the energy dissipation ratio and the pumping time, are discussed in order to investigate the influence of the control parameters. The energy dissipation ratio is referred to as the ratio between the energy dissipated during TET and the initial energy, whereas the pumping time is defined as the time span of TET. As discussed previously, the point $\left(Z_1^{\min}, Z_2^{2*}\right)$ plays an important role, below which the beneficial effect induced by TET disappears. In this context, the energy dissipation ratio can be calculated as:

$$E_{\text{TET}} = \frac{Z_1^{\text{init}} - Z_1^{\text{min}}}{Z_1^{\text{init}}}$$
$$= 1$$
$$- \frac{8}{81} \frac{\left[4 - \left(1 - 3(g^{sn})^2\right)\left(3 - \sqrt{1 - 3(g^{sn})^2}\right)\right]}{g^{3n} E_1^{\text{init}}}$$
$$(42)$$

When the two control parameters g^{sn} and g^{3n} are chosen according to Eqs. (38) and (41), i.e. TET can be initiated, E_{TET} is bounded between $[0, 1]$. The closer E_{TET} is to unity, the more the energy is dissipated during TET.

The corresponding time duration of TET can be derived by rewriting Eq. (35) as:

$$\frac{\partial Z_1}{\partial \tau_1} = -g^{sn} Z_2 \Rightarrow \frac{\partial Z_1}{\partial Z_2}\frac{\partial Z_2}{\partial \tau_1} = -g^{sn} Z_2 \quad (43)$$

assuming that Z_1 is still greater than Z_1^{min} such that the derivative of Z_1 against Z_2 is continuous.

Substituting Eq. (37) into Eq. (43), one obtains:

$$\frac{\frac{27}{16} Z_2^2 - 3 Z_2 + 1 + (g^{sn})^2}{Z_2} dZ_2 = -g^{sn} d\tau_1 \quad (44)$$

Integrating on both sides, one obtains:

$$f(Z_2) = C - g^{sn} \tau_1 \quad (45)$$

where $f(Z_2) = \frac{27}{32} Z_2^2 - 3 Z_2 + \left(1 + (g^{sn})^2\right) \ln(Z_2)$.

The normalised pumping time at slow time scale can be thus derived from Eq. (45) as:

$$T_{\text{pump}} = \frac{f\left(Z_2^{\text{init}}\right) - f\left(Z_2^{2*}\right)}{g^{sn}} \quad (46)$$

Note that T_{pump} is defined in this equation through the slow time scale τ_1.

Figure 4a, b depicts the evolution of the pumping time and the energy dissipation ratio against different values of g^{sn} ranging from 0.001 to the maximally allowed value for TET, i.e. $\sqrt{1/3}$. For each value of g^{sn}, g^{3n} is chosen such that the normalised initial energy Z_1^{init} is 1.1 times greater than the threshold value Z_1^{max} where E_1^{init} is set to 0.01. As shown, both metrics monotonically decrease with an increase of g^{sn}. This means that a large amount of energy is dissipated during TET when g^{sn} is set to a relatively small value, but this comes at the cost of a longer pumping time. Therefore, there is a trade-off in choosing a suitable value of g^{sn} for the considered performance metrics.

Figure 5a, b illustrates the same quantities but against g^{3n} when g^{sn} is set to 0.1. The range of g^{3n} is defined such that the normalised initial energy Z_1^{init} varies from $1.1 \times Z_1^{\text{max}}$ to $5 \times Z_1^{\text{max}}$. Contrary to the previous case, both metrics monotonically increase with an increase of g^{3n}. This means that more energy is dissipated for a greater value of g^{3n}, but again it needs more time to complete. Therefore, the same

Fig. 4 a Pumping time and b energy dissipation ratio against g^{sn} when g^{3n} is chosen so that the initial energy Z_1^{init} is 1.1 times greater than Z_1^{max}
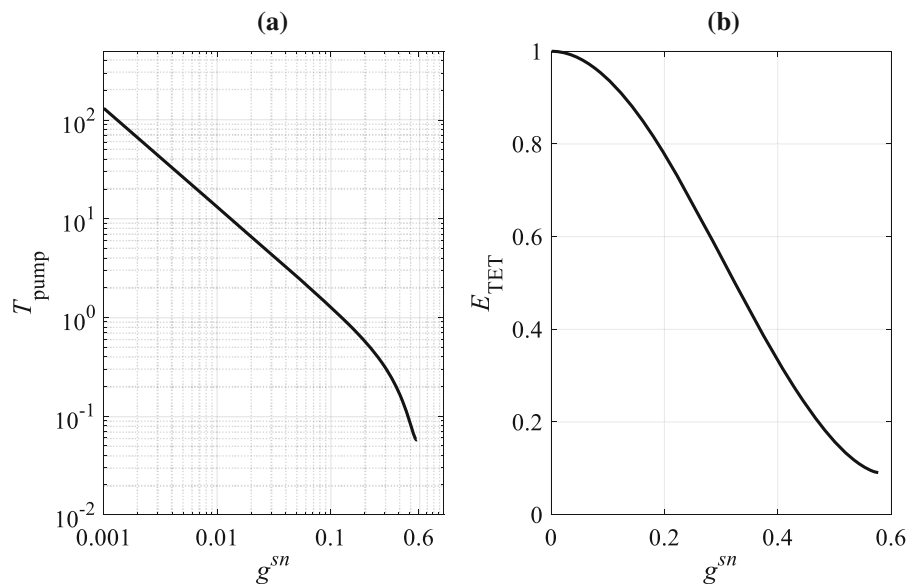
Fig. 5 **a** Pumping time and
b energy dissipation ratio
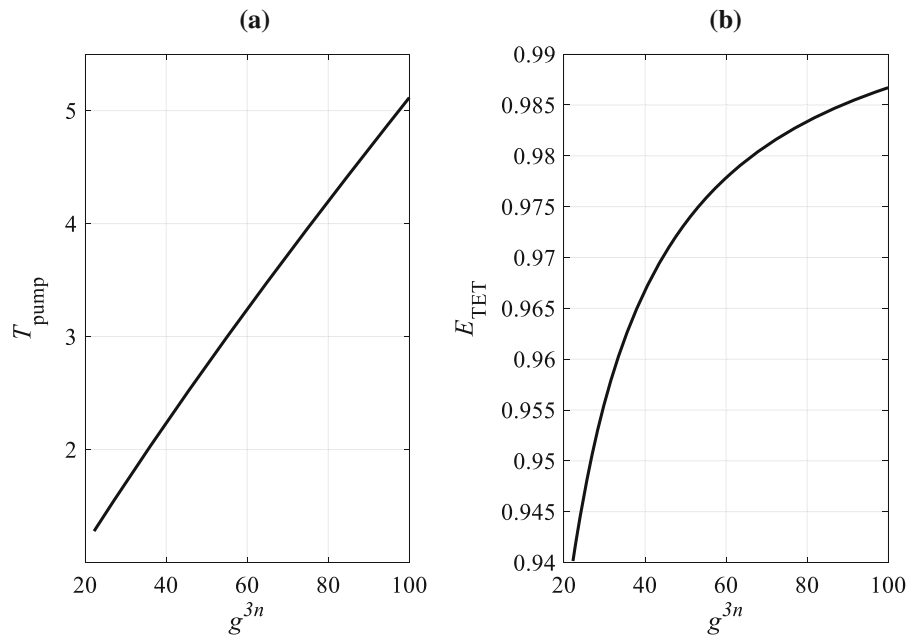against g^{3n} when g^{sn} is set to
0.1

(a)

(b)

Table 1 Parameters used for numerical simulations

System parameters	g^{sn}	g^{3n}	x_1^{init}	ε
TET activated	0.2	2.6×10^3	10^{-2}	0.02
TET inactivated	0.2	1.7×10^3	10^{-2}	0.02

compromise is observed for the choice of g^{3n}. In the
light of Fig. 5a, b, it is recommended to set it is slightly
above the threshold value as the pumping time T_{pump}
degrades more than the energy dissipation rate E_{TET}
benefits from an increase of g^{3n}.

Fig. 6 Comparison of
numerical and analytical
results when TET is
activated for: **a** Z_1 and **b** Z_2
at the slow time scale

(a)

(b)
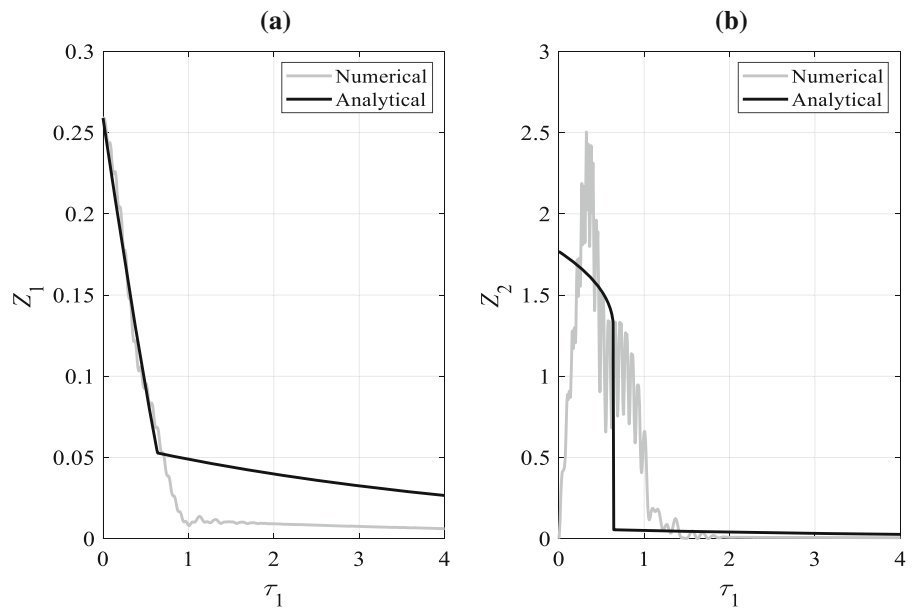
3.3 Numerical validation

Numerical studies are performed in order to validate the derived semi-analytic equations and to examine the control effectiveness of the proposed ANES. The MATLAB built-in integration function *ode45* is used to solve the original governing Eqs. (10) and (11). The solutions are then substituted into Eqs. (31) and (32) in order to compute the energy-like variables E_1 and E_2, and eventually Z_1 and Z_2. The system parameters are listed in Table 1. Two cases are considered, i.e. g^{3n} is chosen to be 1.2 and 0.8 times greater than the minimum value required for triggering TET.

Figure 6 compares the results computed using the numerical and the analytical approach when TET is activated. It can be observed that Z_1 decays with a quasi-linear slope until the critical point at which Z_2 undergoes a jump. In addition, the evolution of Z_1 is shown to be determined only by the slow time scale dynamics as suggested by Eq. (19), whereas Z_2 exhibits both fast and slow-scale dynamics. Despite some differences present after the critical point, the semi-analytical result in terms of Z_1 is found to be in good accordance with that obtained from the numerical calculations. In contrast, Z_2 behaves differently between the numerical and analytical results. This is because the semi-analytical approach neglects the fast
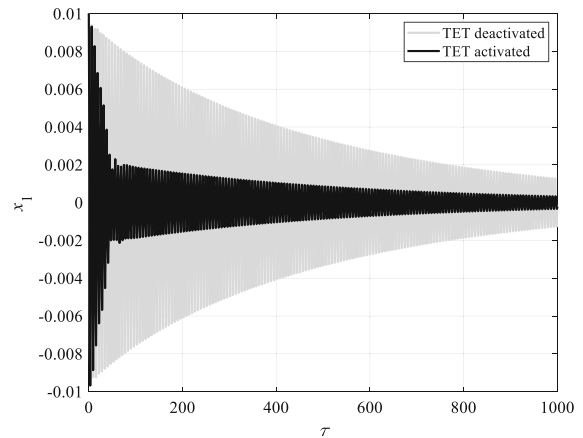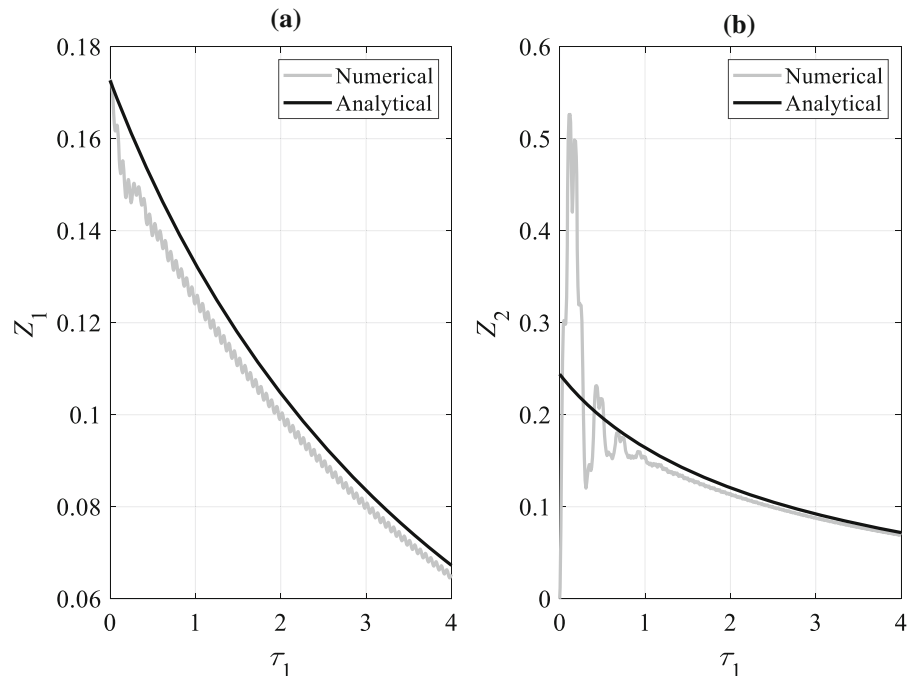

Fig. 8 Comparison of control effectiveness when TET is activated or deactivated

time scale contributions such that it fails to predict the actual dynamics of Z_2. Nevertheless, the semi-analytic solution for Z_2 gives the trend of the response when averaging out the fast components of the actual solutions. It should also be noted that Z_2 exhibits initially some high-frequency oscillations. This is caused by the fact that the initial state of the system does not necessarily lie on the slow invariant manifold such that it takes some time to be attracted to this manifold. This is also referred to as nonlinear beating
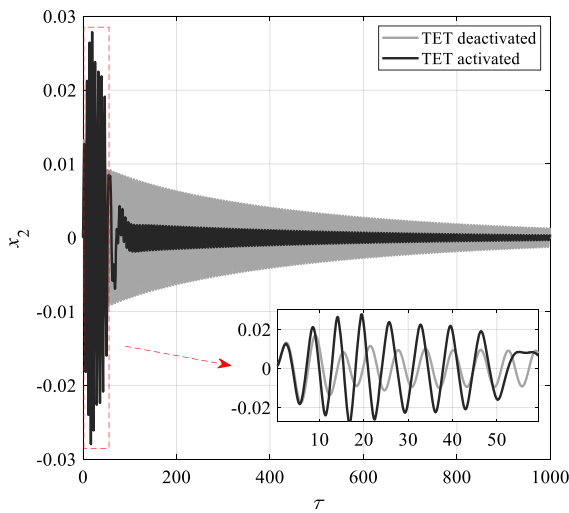
Fig. 7 Comparison of numerical and analytical results when TET is inactive for: **a** Z_1 and **b** Z_2 at the slow time scale

Fig. 9 Comparison of the normalised transmission force x_2 when TET is deactivated or activated
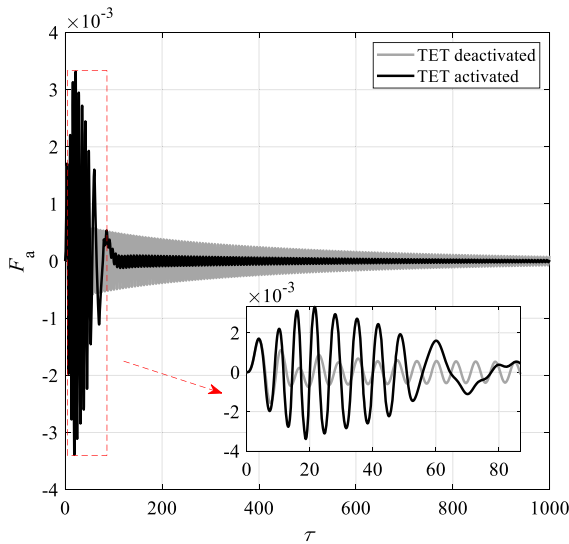

Fig. 10 Comparison of the normalised driving force when TET is deactivated or activated

[10]. The mismatch after the critical point is caused by the fact that the sudden jump of Z_2 is not well followed by the fast dynamics. Overall, the semi-analytical approach is shown to offer a good qualitative description of the system's dynamics.

Figure 7 plots the results obtained when TET is not activated. A fairly good match is observed. Both Z_1 and Z_2 decay with an exponential slope, as linear systems do.

The control performance in terms of the primary structure's displacement is compared in Fig. 8 when TET is activated or not. It is clear that the energy is damped much more quickly when the ANES is tuned to activate TET.

Figure 9 depicts the variable x_2, i.e. the normalised force measured by the force sensor. It can be seen that more energy is pumped into the ANES when TET is activated, as evidenced by the comparison of the oscillation amplitude for the two cases. The corresponding driving forces, i.e.

$$F_a(t) = g^{sn} \int_{t=0}^{t} x_2 \, dt + g^{3n} \int_0^t \int_0^t (x_2)^3 \, dt \, dt, \text{ for the two}$$

cases are plotted in Fig. 10. Accordingly, more forces need to be delivered when TET is activated. Note that x_1, x_2 and F_a shown in Figs. 8, 9 and 10 are dimensionless quantities. In order to implement the proposed ANES for practical applications, special care should be given on the specifications of the transducer and the corresponding amplifiers such that the required stroke and force are satisfied.
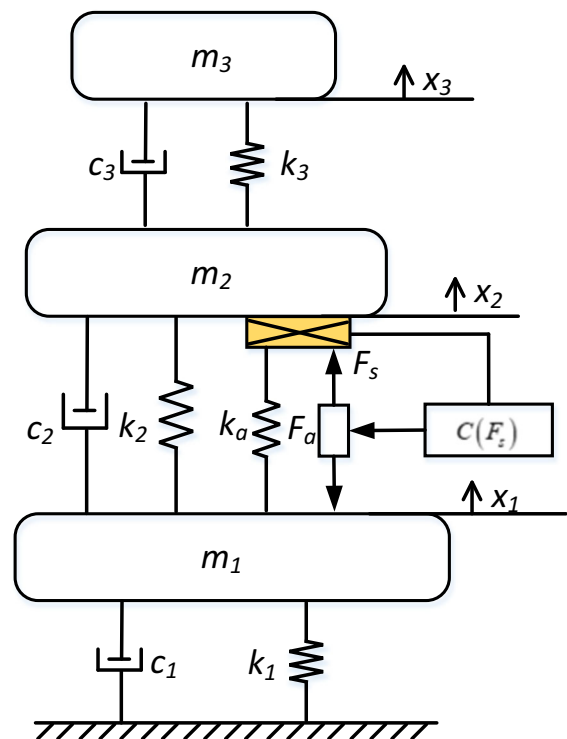

Fig. 11 A linear MDOF system coupled with an ANES

Table 2 Parameters of the primary system

Parameters	Value	Parameters	Value	Parameters	Value
m_1 (kg)	1	m_2 (kg)	1	m_3 (kg)	1
k_1 (N/m)	1	k_2 (N/m)	1	k_3 (Ns/m)	1
c_1 (Ns/m)	0	c_2 (Ns/m)	0	c_3 (Ns/m)	0

4 ANES tuning for MDOF systems

For MDOF systems, another appealing feature of a mechanical NES is the capability of mitigating the vibrations of multiple structural modes. The underlying mechanism is referred to as resonance capture cascade (RCC). In this section, it is shown that an ANES can damp multiple structural modes through RCC and the tuning law for triggering multi-frequency TET is derived.

The considered system is shown in Fig. 11, where a linear three-degree-of-system is taken as the primary structure and an ANES is placed between m_2 and m_1. The parameters of the primary structure are listed in Table 2. The question is how to choose the control parameters g_s and g_{d3} such that multi-frequency TET can be activated for this system. Similar to a mechanical NES, the idea is to assume that ANES interacts with a single structural mode at a time. If so, the guidelines for triggering the occurrence of TET for a SDOF system can be directly applied. The values of g_s and g_{d3} required for activating TET of each mode can be obtained. Then, one can examine whether TET can be triggered for all the structural modes of interest with one single setting of g_s and g_{d3}.

Following upon this idea, the primary system is firstly decomposed into three SDOF systems in modal coordinates. The mass-normalised eigenvector matrix of the primary system and the resonance frequencies are:

$$\mathbf{E} = \begin{bmatrix} 0.328 & -0.737 & 0.591 \\ 0.591 & -0.325 & -0.737 \\ 0.737 & 0.591 & 0.328 \end{bmatrix} \quad (47)$$

$$\boldsymbol{\omega} = \begin{bmatrix} 0.445 \\ 1.247 \\ 1.802 \end{bmatrix} \text{rad/s} \quad (48)$$

The ANES stiffness $k_a = 0.057$ is chosen such that the modal stiffness ratio between the ANES and the

primary system for mode 1 is equal to 2%. According to Eq. (9), the normalised control parameter g^{sn} decreases with the resonance frequency. Therefore, g_s is chosen such that g^{sn} for mode 1 is equal to 2%. In this way, g^{sn} for the other modes is smaller than 2% which automatically meets the condition given by (38). The initial condition of the system $\mathbf{X}^{\text{init}}$ is taken as:

$$\mathbf{X}^{\text{init}} = \begin{bmatrix} x_1, & x_2, & x_3 \end{bmatrix}^{\text{T}} = \begin{bmatrix} 0.01, & 0, & 0 \end{bmatrix}^{\text{T}} \quad (49)$$

The initial condition in the modal coordinates can be obtained:

$$\begin{aligned} \mathbf{Q}^{\text{init}} &= \mathbf{E}^{-1}\mathbf{X}^{\text{init}} \\ &= \begin{bmatrix} 3.3 \times 10^{-3} & -7.4 \times 10^{-3} & 5.9 \times 10^{-3} \end{bmatrix}^{\text{T}} \end{aligned} \quad (50)$$

The mode shape difference at the locations of the ANES, i.e. Δe_i as in Eq. (8), is calculated by taking the difference between the first two rows of the eigenvector $\mathbf{E}$. Grouping them in vector form, one obtains:

$$\begin{aligned} \Delta \mathbf{e} &= \begin{bmatrix} \Delta e_1 & \Delta e_2 & \Delta e_3 \end{bmatrix}^T \\ &= \begin{bmatrix} 0.263 & 0.409 & -1.328 \end{bmatrix}^T \end{aligned} \quad (51)$$

The actuator connection vector $\mathbf{b}$ as defined in Eq. (1) for the considered system is given as:

$$\mathbf{b} = \begin{bmatrix} -1, & 1, & 0 \end{bmatrix}^{\text{T}} \quad (52)$$

where the indices l and k represent the first and the second DOF indices to which the actuator is attached.

With the knowledge of g_s, k_a, $\mathbf{Q}_{\text{int}}$, $\Delta \mathbf{e}$ and $\boldsymbol{\omega}$, the threshold of g_{d3} for triggering each mode's TET, referred to as $\left(g_{d3}^{\min}\right)_i, \forall i = 1, 2, 3$, can be derived by substituting these parameters into Eqs. (41), (9) and (8). The results are given in Table 3. It is found that $\left(g_{d3}^{\min}\right)_1$ for mode 1 is greater than that for the other two modes. This implies that TET can be triggered for all modes if g_{d3} is greater than $\left(g_{d3}^{\min}\right)_1$. The final value of g_{d3} is thus set to be 1.2 times greater than $\left(g_{d3}^{\min}\right)_1$, completing the determination of the ANES parameters g_s, g_{d3} and k_a.

The ANES performance is preliminarily assessed by using the two performance indices, i.e. the pumping time T_{pump} and the energy dropping ratio E_{TET}. Their values are listed in Table 3. It is seen that it takes around 415 s for pumping out the energy associated with mode 2, while only 71 s are required for mode 1. This is mainly because the effective stiffness ratio and

Table 3 ANES parameters and performance measures

Parameters	$(g^{sn})_i$	$(Z_1^{\max})_i$	ε_i	$(g_{d3}^{\min})_i$	$(g^{3n})_i$	$(Z_1^{\text{init}})_i$	$(T_{\text{pump}})_i$	$(E_{\text{TET}})_i$
Mode 1	0.2	0.216	0.02	1.8×10^7	2.4×10^4	0.259	71.6 s	79.6%
Mode 2	0.07	0.2	0.006	1.0×10^7	7.4×10^3	0.403	415.8 s	98.3%
Mode 3	0.05	0.199	0.03	3.2×10^6	3.7×10^4	1.308	234.9 s	99.7%
ANES	$g_s = 0.09$			$g_{d3} = 2.1 \times 10^7$			$k_a = 0.057$ N/m	
ATID	$g_s = 0.62$			$g_d = 0.32$			$k_a = 0.057$ N/m	

the damping ratio for the second mode are relatively low. During TET, the energy possessed by modes 2 and 3 is almost completely dissipated by the ANES, while approximately 80% of the energy is damped out for mode 1. This is caused by the fact that the damping ratio for the first mode is relative high and the corresponding initial value Z_1^{init} is close to the threshold $Z_1^{\max}$.

In order to verify the analytical analysis, a numerical simulation is performed for the coupled system. Figure 12a, b plot the time history and the time–frequency analysis of the transmission force F_s, respectively. As can be seen, the ANES is able to interact with each mode sequentially. Once a sufficient amount of energy has been dissipated, the ANES escapes from the current resonance capture and engages with the next mode, realising in essence a RCC. The comparison between Fig. 12a and Table 3 highlights that the pumping time for each mode is correctly predicted by the analytical results. The vibration mitigation performance is evaluated by the response of m_1, the results of which are shown in Fig. 12c, d, respectively. Interestingly, it is seen that the energy associated with each mode is dissipated only when the corresponding TET occurs, again confirming the previous assumption. A benchmark case is considered where g_{d3} is set to 1% of the current value such that no TETs are triggered. The resulting control performance in terms of the displacement of m_1 is superimposed in Fig. 12c. The comparison clearly highlights the vibration mitigation efficiency improved by the well-tuned ANES.

Next, the control effectiveness of the ANES is also compared with that of a linear active tuned inerter damper (ATID) [23] on the considered primary system. The relationship between an ATID and an ANES can be understood in analogy with a mechanical TMD and a mechanical NES. The ATID is configured such that the effective damping associated with mode 1 is maximised according to the tuning law in [34]. The corresponding control parameters, i.e. gains of the single integrator g_s and the double integrator g_d, are given in Table 3. The resulting control performance is shown in Fig. 13 which is superimposed with that of the ANES. Figure 14 plots the time–frequency distribution of x_1 when the optimally configured ATID is used. As shown in Fig. 13, the ATID seems to outperform the ANES in the time window between 150 and 600 s. In fact, the vibrations when ANES is used during this period are mainly due to two vibration modes (mode 1 & mode 2), as seen from the time–frequency plot in Fig. 12d. As ANES takes effect sequentially from high modes to low modes, in this time window, ANES affects only mode 2 and basically leaves mode 1 'undamped'. On the other hand, the vibrations associated with mode 1 for ATID start to be attenuated from the very beginning. When the time reaches 200 s, the energy with mode 1 is already well dissipated and the vibrations are basically dominated by mode 2, which is not effectively damped by the ATID. The results show clearly that ANES can effectively damp the energy of all the modes of the system, while ATID can only be tuned to one mode. This broadband efficiency of ANES makes it also much more robust to the presence of uncertainties in the primary system as demonstrated by the comparison between a mechanical NES and a mechanical TMD in [10].

5 Conclusion

This paper discussed an active nonlinear energy sink concept realised by a pair of collocated reactive actuator and force sensor. The equivalent mechanical representation, i.e. serially-connected cube root inerter, linear damper and linear spring, has been derived to better understand the physics behind the coupled
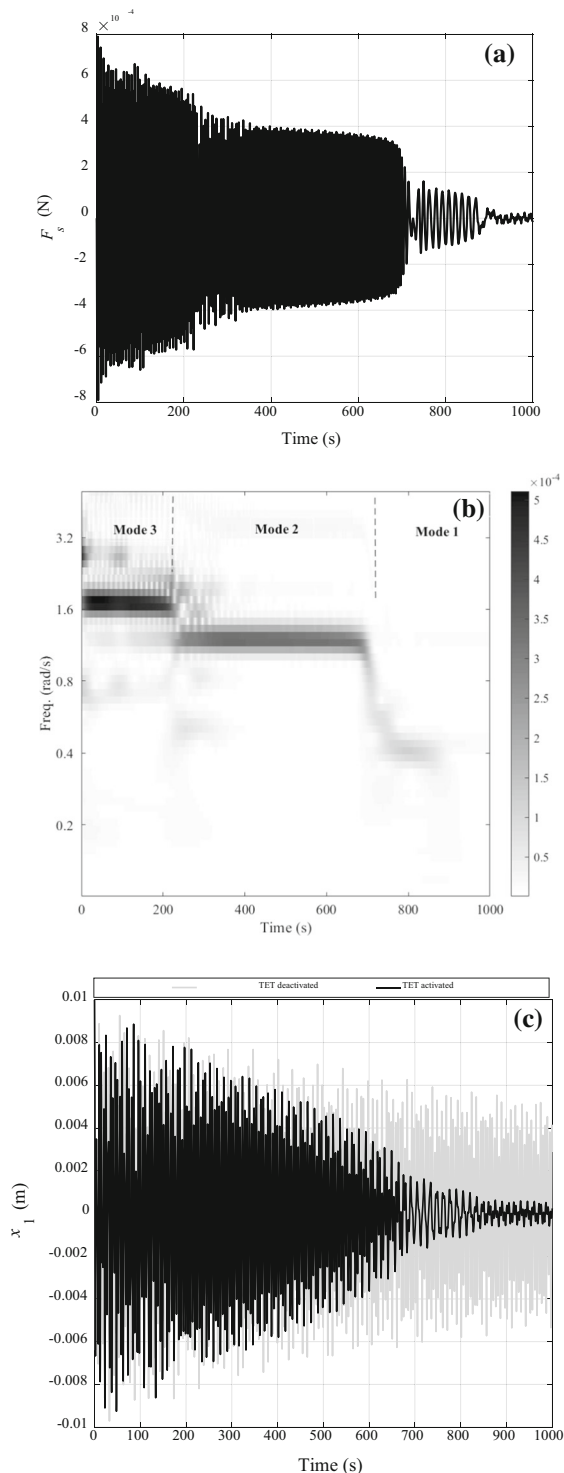
Fig. 12 continued

Fig. 13 Control effectiveness comparison between ANES and ATID

Fig. 12 **a** time history of the transmission force F_s; **b** time–frequency distribution of F_s; **c** time history of x_1; **d** time–frequency distribution of x_1
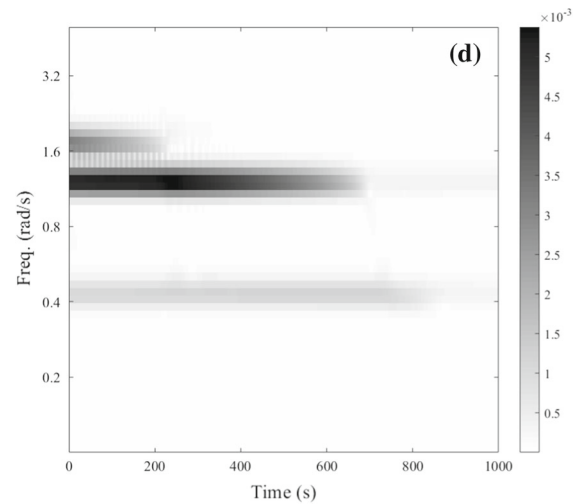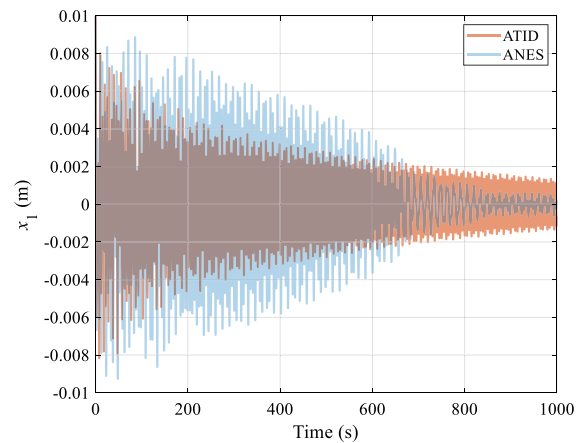
electromechanical system. It is found that an ANES and a NES behave similarly in terms of their slow-scale dynamics and vibration mitigation effectiveness. Closed-form tuning laws for regulating the control parameters of the ANES have been derived for both SDOF and MDOF systems. The well-known threshold in terms of the host structure vibration's energy for triggering TET is converted into constraints on the control parameters which allows a straightforward implementation in practice. The influence of the control parameters on the vibration mitigation performance has also been investigated. More energy is dissipated during TET if the control parameter g_s is relatively small, but it takes more time to do so. An
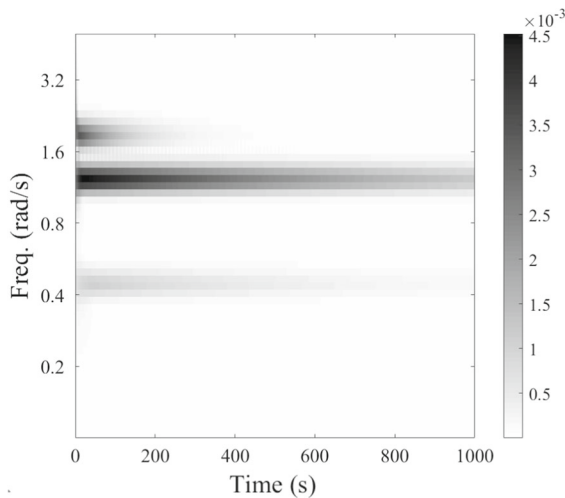
Fig. 14 Time-frequency distribution of x_1 when the optimally configured ATID is used

opposite trend applies for the other control parameter g_{d3}. Numerical simulations have been performed to verify the analytical developments. From a practical viewpoint, the proposed ANES is preferable over a mechanical NES as it not only features real-time tuning of the control parameters, but also allows for a flexible implementation of various forms of the nonlinear exponent. In addition, one can envision to develop an analogue electronic control system for the collocated actuator-force sensor pair such that the resulting ANES would be compact enough for smart structure applications.

Compliance with ethical standards

Conflict of interest The authors declare that they have no conflict of interest.

Appendix A

In this appendix, it is shown that the systems sketched in Fig. 1a, b are dynamically equivalent, or, in other words, the networks shown in Fig. 15a, b are equivalent.

Figure 15b depicts a pure mechanical system which consists of a cube root inerter, a dashpot and a spring connected in series. A cube root inerter impedes the

relative acceleration across its terminals with a force proportional to the cube root of its relative acceleration. Under the excitation force denoted by F, the governing equations of this system can be written as:

$$F = -m_a \sqrt[3]{\ddot{x}_1 - \ddot{x}_2} \tag{53}$$

$$F = -d_a(\dot{x}_2 - \dot{x}_3) \tag{54}$$

$$F = -k_a(x_3 - x_4) \tag{55}$$

where $x_i, \forall i = 1, 2, 3, 4$ denotes the node displacement of each mechanical component.

Expressing the relative motion in terms of the transmission force F, Eqs. (53)–(55) can be rewritten as:

$$-\int_0^t \int_0^t \left(\frac{F}{m_a}\right)^3 \mathrm{d}t\mathrm{d}t = x_1 - x_2 \tag{56}$$

$$-\int_0^t \frac{F}{d_a}\mathrm{d}t = x_2 - x_3 \tag{57}$$

$$-\frac{F}{k_a} = x_3 - x_4 \tag{58}$$

Summing up Eqs. (56)–(58) and multiplying both sides with k_a, yields:

$$-\frac{k_a \iint F^3}{m_a^3} - \frac{k_a \int F}{d_a} - F = k_a(x_1 - x_4) \tag{59}$$

According to the control law, the governing equations of the system shown in Fig. 15a can be expressed as:

$$F = -g_s \int_0^t F\mathrm{d}t - g_{d3} \int_0^t \int_0^t F^3\mathrm{d}t\mathrm{d}t - k_a x \tag{60}$$

where $x = x_1 - x_4$ represents the relative displacement across the ANES.

Comparing Eq. (59) with Eq. (60), one can find the equivalence between systems shown in Fig. 15a, b. The feedback gains and their corresponding mechanical components are thus related by the following equation:

$$d_a = k_a/g_s; \quad m_{a3} = \sqrt[3]{k_a/g_{d3}} \tag{61}$$

Fig. 15 **a** the sketch of the active system and **b** its mechanical representative

(a)   (b)
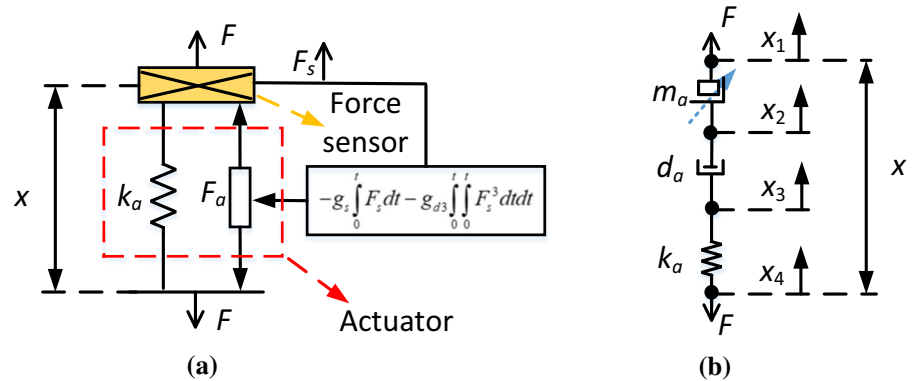
References

1. Wang, F.-Y., Gao, Y.: Advanced Studies of Flexible Robotic Manipulators. World Scientific, Singapore (2003)

2. Darecki, M., Edelstenne, C., Enders, T., Fernandez, E., Hartman, P., Herteman, J.-P., Kerkloh, M., King, I., Ky, P., Mathieu, M., Orsi, G., Schotman, G., Smith, C., Wörner, J.-D.: Flightpath 2050. Flightpath 2050 Eur. Vis. Aviat. 28 (2011). https://doi.org/10.2777/50266

3. Den Hartog, J.P.: Mechanical Vibrations. Dover Publications, New York (1985)

4. Warburton, G.B.G.: Optimum absorber parameters for various combinations of response and excitation parameters. Earthq. Eng. Struct. Dyn. **10**, 381–401 (1982). https://doi.org/10.1002/eqe.4290100304

5. von Flotow, A.H., Beard, A., Bailey, D.: Adaptive tuned vibration absorbers: tuning laws, tracking agility, sizing, and physical implementations. In: Adaptive Tuned Vibration Absorbers: Tuning Laws, Tracking Agility, Sizing, and Physical Implementations, pp. 437–454. Noise-con 94, Fort Lauderdale, New York (1994)

6. Gendelman, O., Manevitch, L.I., Vakakis, A.F., Mcloskey, R.: Energy pumping in nonlinear mechanical oscillators: Part I—dynamics of the underlying hamiltonian systems. J. Appl. Mech. Trans. ASME **68**, 34–41 (2001). https://doi.org/10.1115/1.1345524

7. Vakakis, A.F., Gendelman, O.: Energy pumping in nonlinear mechanical oscillators: Part II—resonance capture. J. Appl. Mech. Trans. ASME **68**, 42–48 (2001). https://doi.org/10.1115/1.1345525

8. Lee, Y.S., Kerschen, G., Vakakis, A.F., Panagopoulos, P., Bergman, L., McFarland, D.M.: Complicated dynamics of a linear oscillator with a light, essentially nonlinear attachment. Phys. D Nonlinear Phenom. **204**, 41–69 (2005). https://doi.org/10.1016/j.physd.2005.03.014

9. Kerschen, G., Lee, Y.S., Vakakis, A.F., Mcfarland, D.M., Bergman, L.A.: Irreversible passive energy transfer in coupled oscillators with essential nonlinearity. SIAM J. Appl. Math. **66**, 648–679 (2006). https://doi.org/10.1137/040613706

10. Vakakis, A.F., Gendelman, O.V., Bergman, L.A., McFarland, D.M., Kerschen, G., Sup, L.Y.: Nonlinear Targeted Energy Transfer in Mechanical and Structural Systems. Springer, Berlin (2008)

11. Ture Savadkoohi, A., Vaurigaud, B., Lamarque, C.-H., Pernot, S.: Targeted energy transfer with parallel nonlinear energy sinks, part II: theory and experiments. Nonlinear Dyn. **67**, 37–46 (2012). https://doi.org/10.1007/s11071-011-9955-z

12. Vaurigaud, B., Ture Savadkoohi, A., Lamarque, C.H.: Targeted energy transfer with parallel nonlinear energy sinks Part I: Design theory and numerical results. Nonlinear Dyn. **66**, 763–780 (2011). https://doi.org/10.1007/s11071-011-9949-x

13. Tripathi, A., Grover, P., Kalmár-Nagy, T.: On optimal performance of nonlinear energy sinks in multiple-degree-of-freedom systems. J. Sound Vib. **388**, 272–297 (2017). https://doi.org/10.1016/j.jsv.2016.10.025

14. Nguyen, T.A., Pernot, S.: Design criteria for optimally tuned nonlinear energy sinks-part 1: Transient regime. Nonlinear Dyn. **69**, 1–19 (2012). https://doi.org/10.1007/s11071-011-0242-9

15. Dekemele, K., De Keyser, R., Loccufier, M.: Performance measures for targeted energy transfer and resonance capture cascading in nonlinear energy sinks. Nonlinear Dyn. **93**, 259–284 (2018). https://doi.org/10.1007/s11071-018-4190-5

16. Qiu, D., Seguy, S., Paredes, M.: Design criteria for optimally tuned vibro-impact nonlinear energy sink. J. Sound Vib. **442**, 497–513 (2019). https://doi.org/10.1016/j.jsv.2018.11.021

17. Zhang, Z., Lu, Z.Q., Ding, H., Chen, L.Q.: An inertial nonlinear energy sink. J. Sound Vib. **450**, 199–213 (2019). https://doi.org/10.1016/j.jsv.2019.03.014

18. Javidialesaadi, A., Wierschem, N.E.: An inerter-enhanced nonlinear energy sink. Mech. Syst. Signal Process. **129**, 449–454 (2019). https://doi.org/10.1016/j.ymssp.2019.04.047

19. Smith, M.C.: Synthesis of mechanical networks: the inerter. IEEE Trans. Automat. Control **47**, 1648–1662 (2002). https://doi.org/10.1109/TAC.2002.803532

20. Chen, M.Z.Q., Papageorgiou, C., Scheibe, F., Wang, F.C., Smith, M.: The missing mechanical circuit element. IEEE Circuits Syst. Mag. **9**, 10–26 (2009). https://doi.org/10.1109/MCAS.2008.931738

21. Preumont, A., François, A., Bossens, F., Abu-Hanieh, A.: Force feedback versus acceleration feedback in active

vibration isolation. J. Sound Vib. **257**, 605–613 (2002). https://doi.org/10.1006/jsvi.2002.5047

22. Zhao, G., Raze, G., Paknejad, A., Deraemaeker, A., Kerschen, G., Collette, C.: Active nonlinear inerter damper for vibration mitigation of Duffing oscillators. J. Sound Vib. **473**, 115236 (2020). https://doi.org/10.1016/j.jsv.2020.115236

23. Zhao, G., Raze, G., Paknejad, A., Deraemaeker, A., Kerschen, G., Collette, C.: Active tuned inerter-damper for smart structures and its $\mathcal{H}_\infty$ optimisation. Mech. Syst. Signal Process. **129**, 470–478 (2019). https://doi.org/10.1016/j.ymssp.2019.04.044

24. Zhao, G., Paknejad, A., Deraemaeker, A., Collette, C.: $\mathcal{H}_\infty$ optimization of an integral force feedback controller. J. Vib. Control **25**, 2330–2339 (2019). https://doi.org/10.1177/1077546319853165

25. Sun, K., Liu, L., Qiu, J., Feng, G.: fuzzy adaptive finite-time fault-tolerant control for strict-feedback nonlinear systems. IEEE Trans. Fuzzy Syst. (2020). https://doi.org/10.1109/TFUZZ.2020.2965890

26. K., S., Jianbin, Q., Karimi, H.R., Fu, Y.: Event-triggered robust fuzzy adaptive finite-time control of nonlinear systems with prescribed performance. IEEE Trans. Fuzzy Syst. (2020). https://doi.org/10.1109/TFUZZ.2020.2979129

27. Sun, K., Qiu, J., Karimi, H.R., Gao, H.: A novel finite-time control for nonstrict feedback saturated nonlinear systems with tracking error constraint. IEEE Trans. Syst. Man Cybern. Syst. (2020). https://doi.org/10.1109/TSMC.2019.2958072

28. Slotine, J.-J., Li, W.: Applied Nonlinear Control. Prentice Hall, Michigan (1991)

29. Preumont, A.: Vibration Control of Active Structures. Springer, Netherlands, Dordrecht (2011)

30. Manevitch, L.: Complex representation of dynamics of coupled nonlinear oscillators. Mathematical Models of Non-linear Excitations. Transfer, Dynamics, and Control in Condensed Systems and Other Media, pp. 269–300. Kluwer Academic, Tver, Russia (1999)

31. Nayfeh, A.H., Mook, D.T.: Nonlinear Oscillations. Wiley-VCH Verlag GmbH, Weinheim, Germany (1995)

32. Gendelman, O.V.: Bifurcations of nonlinear normal modes of linear oscillator with strongly nonlinear damped attachment. Nonlinear Dyn. **37**, 115–128 (2004). https://doi.org/10.1023/B:NODY.0000042911.49430.25

33. Habib, G., Detroux, T., Viguié, R., Kerschen, G.: Nonlinear generalization of Den Hartog's equal-peak method. Mech. Syst. Signal Process. **52–53**, 17–28 (2015). https://doi.org/10.1016/j.ymssp.2014.08.009

34. Chesné, S., Milhomem, A., Collette, C.: Enhanced damping of flexible structures using force feedback. J. Guid. Control Dyn. **39**, 1654–1658 (2016). https://doi.org/10.2514/1.G001620